Optimal GNSS-Based Passive SAR Large Field-of-View Imaging via Multistatic Configuration: Method and Experimental Validation

Chuan Huang, *Student Member, IEEE*, Zhongyu Li, *Member, IEEE*, Hongyang An, *Member, IEEE*, Zhichao Sun, *Member, IEEE*, Junjie Wu, *Member, IEEE*, and Jianyu Yang, *Member, IEEE*

***Abstract*—In terms of the global coverage provided by global navigation satellite system (GNSS) signals, radar images of a large field-of-view can be obtained via passive synthetic aperture radar (SAR) using these signals of opportunity. Usually, large field-of-view imaging is challenging using conventional SAR methods owing to the space-variant resolution. In addition, only a moderate range resolution can be provided by the GNSS transmitters in the passive SAR system. In this article, an optimal imaging method for a large field-of-view using GNSS-based passive SAR is proposed, which exploits the inherent multistatic nature of GNSS. At first, the spatial resolution of each scatterer in the observation area relative to each GNSS transmitter is calculated according to the geometry. Then, the selection of the transmitter set is modeled as an optimization problem, where the minimal resolution cell is used as the optimal criterion. After that, an evolutionary algorithm is applied to solve the optimization problem. Finally, the space-time combination of the echoes over a long dwell time concerning selected GNSS transmitters is performed to form the radar image with a minimal spatial resolution. The proposed method is extensively validated using two experimental datasets, where the passive radar consists of BeiDou satellites and a fixed receiver. The spatial resolution improvement and the large field-of-view imaging capability of the proposed method are forcefully demonstrated according to the experimental results.**

***Index Terms*—Large field-of-view, multistatic radar, passive radar, satellite signals of opportunity, synthetic aperture radar.**

I. Introduction

OVER the last decades, the synthetic aperture radar (SAR) has become one of the most popular tools for earth surface monitoring since it enables to obtain day and night-time images of the observed areas with all-weather conditions [1]. As a special system construction, the passive SAR uses the transmitters of opportunity for scene illumination [2]. The lack of dedicated radar transmitters significantly reduces its cost and size. Some other advantages, such as antijamming and anti-stealth capabilities, can be introduced to passive SAR owing to its inherent bistatic or even multistatic configuration. Furthermore, such a radar system is green since electromagnetic pollution can be avoided and a spectrum allocation is not needed [3], [5], [6].

In the last few years, there is a growing interest in passive SAR system. Currently, some terrestrial sources, such as digital video broadcast-terrestrial (DVB-T) and global system for mobile communications , have been exploited for the passive imaging purpose [7], [8], [9], [10]. Since these kinds of opportunistic illuminators are usually fixed, the virtual apertures are formed with moving receiving platforms, such as aircraft and unmanned aerial vehicle. However, as the signal coverage is confined by its fixed base station, the application scenario of the passive SAR system utilizing a terrestrial source is limited. In addition, the bandwidths of these signals are usually restricted (e.g., 7.6 MHz for DVB-T signal) [8], which may result in insufficient range resolution of the acquired radar image.

To address the abovementioned limitations, one of the promising alternatives exploited for passive SAR system can be the global navigation satellite system (GNSS). There are several advantages to choosing this opportunistic transmitter. First, the GNSS ensures a global and permanent signal availability on the earth's surface even at the poles [11]. Thus, the coverage of the GNSS-based passive SAR only depends on the position and beamwidth of the receiver, which can meet more application scenarios. Then, the GNSS provides a relatively larger signal bandwidth (up to 20 MHz) than the terrestrial sources [12]. Thus the constituted passive SAR enables to provide a better spatial resolution. In addition, it is noted that there are currently four GNSS constellations built or under construction, i.e., GPS, GLONASS, Galileo, and BeiDou [13], [14]. Each GNSS constellation operates at least 24 navigation satellites in medium earth orbit (MEO). Some satellites are even in geostationary earth orbit and inclined geosynchronous orbit (IGSO) [15]. These satellites are hard to destroy, providing stable and persistent signal sources. More importantly, given the positioning intent of GNSS, a scene of interest is simultaneously illuminated by 4–8 satellites in a single GNSS constellation [16].

Manuscript received 31 July 2022; revised 12 September 2022 and 21 October 2022; accepted 7 November 2022. Date of publication 10 November 2022; date of current version 23 November 2022. This work was supported in part by the National Natural Science Foundation of China under Grant 62171084, Grant 62101096, Grant 61901088, and Grant 61922023 and in part by the Postdoctoral Innovation Talent Support Program under Grant BX2021058. *(Corresponding author: Zhongyu Li.)*

The authors are with the School of Information and Communication Engineering, University of Electronic Science and Technology of China, Chengdu 611731, China (e-mail: huangchuan@std.uestc.edu.cn; zhongyu_li@hotmail.com; anhongyanga@163.com; threadkite@sina.com; junjie_wu@uestc.edu.cn; jyyang@uestc.edu.cn).

Digital Object Identifier 10.1109/JSTARS.2022.3221214

Since the GNSS constellation operates in code or frequency division approach, signals transmitted from different satellites in view can be collected and separated by a same receiver. That is, the GNSS-based passive SAR is inherently a multistatic SAR system comprising a single receiver and multiple GNSS satellites.

In this article, we focus on GNSS-based passive SAR with a ground-based fixed receiver. It is envisaged here to equip the receiver with a wide-beam antenna, enabling a continuously coverage of a surveyed area with a large field-of-view. There are two main problems in GNSS-based SAR large field-of-view imaging. One of them comes from the GNSS transmitter. Even though the GNSS signal has a relatively larger bandwidth than other opportunistic sources, it is still inferior to a dedicated SAR transmitter [17], [18], [19]. Only a moderate range resolution can be provided by the constituted passive SAR system. On the other hand, the large field-of-view imaging can be a challenging task for a SAR system, since the space-variant resolution is evident and it is difficult to guarantee a fine resolution for each pixel in the surveyed area.

Due to these specific benefits offered by GNSS, currently there have been already several investigations that aim at achieving radar imaging using the GNSS-based SAR. In [12], the imaging processing chain for the passive bistatic SAR using a GNSS transmitter has been described. And the feasibility of GNSS-based passive SAR has been extensively demonstrated via sets of experimental data collected using Galileo and GLONASS transmitters. Then, the passive bistatic SAR using the BeiDou satellite as the transmitter has been constructed in [20] to obtain the corresponding radar image. However, these mentioned researches are only for bistatic configuration with a single satellite transmitter. To take full advantage of GNSS, the availability of multiple navigation satellites is exploited in [21] and [22]. The bistatic images concerning different satellites are generated separately, followed by the multistatic image formation by noncoherently combining the bistatic images. The experimental results show that the multistatic image acquires more information about the surveyed area. However, the combination of bistatic images does not always enhance imaging performance, where the multistatic result strictly relies on each of the bistatic geometries. In [23], GNSS-based SAR imaging performance improvement is achieved via image fusion. After region segmentation of the formed bistatic images, the images are fused using the mean operator or mean operator. But this method is an image fusion strategy in essence, and the special nature of the SAR system is not considered. Moreover, these existing literatures only focus on a limited surveyed area, and these methods are not applicative with respect to a scene with a large view-of-view.

In this article, we aim to robustly achieve GNSS-based passive SAR image of a large field-of-view by resorting to its natural multistatic configuration. Given the restricted power budget from GNSS satellites, the dwell time on the surveyed scene can be extended to several minutes to obtain sufficient echo energy. At the same time, the azimuth resolution of the passive SAR system can be improved with the increase of the synthetic aperture. To obtain a reliable radar image of the large field-of-view, at first in this article, the theoretical bistatic resolutions of each pixel in the imaging plane concerning all the available satellite transmitters are calculated according to their trajectories. Then, with respect to each pixel, a subset of the available transmitters is selected, which aims to improve the resolution. The selection of the transmitter set is modeled as an optimization problem, where the minimal resolution cell of the final image is used as the optimal criterion. And an evolutionary algorithm is applied to solve the optimization problem. Finally, after data separation, each pixel is formed by combining the long-time echoes from the selected GNSS satellites. The proposed method is extensively validated on two experimental datasets, in which the BeiDou satellites are considered the opportunistic transmitters. The main contributions of this article are as follows.

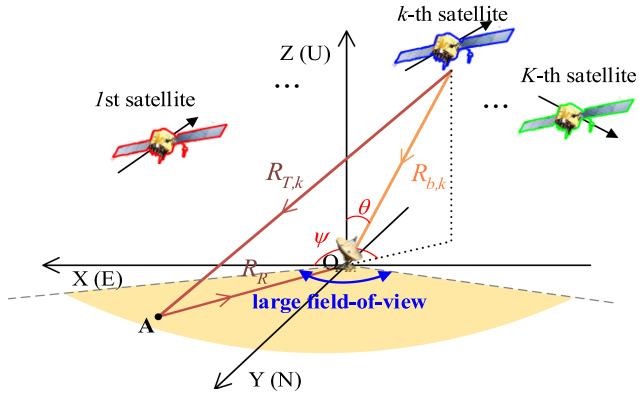

Fig. 1. Topology of GNSS-based passive SAR.

1) The GNSS transmitter set selection strategy based on the criterion of a minimal resolution cell is proposed. The satellite selection is modeled as an optimization problem and solved by an evolutionary algorithm, after which the final radar image is formed by combining the echoes from the selected transmitters.
2) The effectiveness of the proposed method is validity demonstrated using two experimental datasets. In the first experiment, a transponder was treated as a strong point target. The results quantitatively show the resolution improvement of the proposed method. In the other experiment, the large field-of-view imaging capability of the proposed method is demonstrated as the surveyed area with a large field-of-view can be well imaged using the BeiDou-based passive SAR.

The remainder of the article is organized as follows. Section II deduces the signal model of the GNSS-based passive SAR. Section III introduces the scheme of the optimal imaging method. The radar images obtained in the two experiments mentioned above are presented in Section IV. Finally, in Section V, we draw our conclusion.

II. Signal Model

The GNSS-based passive SAR comprises K navigation satellites in view and a ground-based fixed receiver, and its topology is shown in Fig. 1. As a passive radar system with noncooperative transmitters, the receiver equips with two antennas. One of the antennas is steered toward the sky (refer to as reference

antenna), recording the direct signals from the satellites for synchronization purpose. The other antenna (refer to as surveillance antenna) is used to record the reflected signals from the surveyed area. To obtain a sufficient SNR for the passive radar imaging purpose, the dwell time on the surveyed area is on the order of minutes. Such a long time is readily achieved owing to the system components with a fixed receiver and satellite transmitters in the middle or high orbits. It is noted again that the signals transmitted from the different navigation satellites are simultaneously recorded by the receiver and can be separated owing to the employment of code or frequency division. As shown in this figure, the positions of the satellite transmitters and the passive receiver are described in an East-North-up reference system, where the fixed receiver is considered as the origin. The kth satellite locates at $\mathbf{P}_{\mathbf{T},k}$ at reference instant, moving with a velocity vector $\mathbf{v}_{\mathbf{T},k}$.

The imaging quality of each bistatic radar image can be assessed by its spatial resolution. Here, the spatial resolution is calculated by the generalized ambiguity function (GAF) [24]. Let $\mathbf{A}$ denote the position vector of a point scatterer to be evaluated and $\mathbf{B}$ be the position of an arbitrary point in the vicinity of $\mathbf{A}$. Since the receiver is fixed, the GAF is given by

$$|\chi_k(\mathbf{A},\mathbf{B})| = \rho\left(\frac{(\mathbf{\Phi_{TA},}_k + \mathbf{\Phi_{RA}})(\mathbf{B}-\mathbf{A})^{\mathbf{T}}}{c}\right) m \times \left(\frac{\boldsymbol{\omega}_{\mathbf{TA},k}(\mathbf{B}-\mathbf{A})^{\mathbf{T}}}{\lambda}\right) \quad (1)$$

where $(\cdot)^{\mathbf{T}}$ is the transpose of a vector. $\rho(\cdot)$ is the matched filter output of the ranging code for the GNSS signal. It is a triangular function with a pulsewidth twice of the code chip duration. $m(\cdot)$ is inverse Fourier transform of the signal magnitude pattern, and it is a sin$c$ function when the antenna pattern is considered as a rectangle shape. c is the light speed. λ is the wavelength. f_c is the carrier frequency. $\mathbf{\Phi_{TA,k}}$ and $\mathbf{\Phi_{RA}}$ are the unit vectors in the directions from the scatterer $\mathbf{A}$ to the kth satellite and the receiver, respectively. $\boldsymbol{\omega}_{\mathbf{TA},k}$ is the angular velocity of the kth satellite, which is expressed as

$$\boldsymbol{\omega}_{\mathbf{TA},k} = \frac{\mathbf{v}_{\mathbf{T},k}\left(\mathbf{I} - \mathbf{\Phi}_{\mathbf{TA},k}^{\mathbf{T}}\mathbf{\Phi}_{\mathbf{TA},k}\right)}{\|\mathbf{P}_{\mathbf{T},k} - \mathbf{A}\|} \quad (2)$$

where $\|\cdot\|$ is the norm of a vector and $\mathbf{I}$ is the identity matrix.

Usually, the -3 dB width of the GAF is used to quantitatively evaluate the spatial resolution of a radar image, which is defined as resolution cell. Given the extreme asymmetry configuration of the GNSS-based SAR due to greatly far distance between the satellite transmitter and the surveyed area, special property of the space-variant resolution is exhibited. The unit vector $\mathbf{\Phi_{TA,k}}$ is approximately constant for each scatterer in scene, even considering a large field-of-view. Further, the angular velocity $\boldsymbol{\omega}_{\mathbf{TA},k}$ is considered constant. Therefore, it is deduced from (1) that, with respect to a same GNSS transmitter, the resolution cell is only determined by $\mathbf{\Phi_{RA}}$ (or the receiver view angle denoted by ϕ_A).

Furthermore, the GAF in (1) also shows that the bistatic resolution strictly depends on the transmitter's position and trajectory. Thus, passive bistatic images with different resolutions can be achieved using spatially separated satellites. A simulation is used here to demonstrate the dependence of resolution on transmitter. A point scatterer located at (0, -1000) m is assumed in the simulation as an example. Three GNSS satellites are considered as the transmitters, where their trajectories are generated according to actual ephemeris data. The corresponding parameters are calculated and given in Table I. The dwell time on the scatterer stays 10 min. The chip rate of the transmitted signal is set as 10.23 MHz.

TABLE I
PARAMETERS OF THE SATELLITE TRANSMITTERS

	$\mathbf{\Phi_{TA,}}_k$	$\boldsymbol{\omega}_{\mathbf{TA,k}}$
1	(-0.50,0.34,0.80)	(3.00,4.22,0.07)×10^{-5} rad/s
2	(-0.40,0.50,0.77)	(7.48,-4.96,7.13)×10^{-5} rad/s
3	(-0.31,-0.68,0.66)	(3.18,-4.16,-5.82)×10^{-5} rad/s

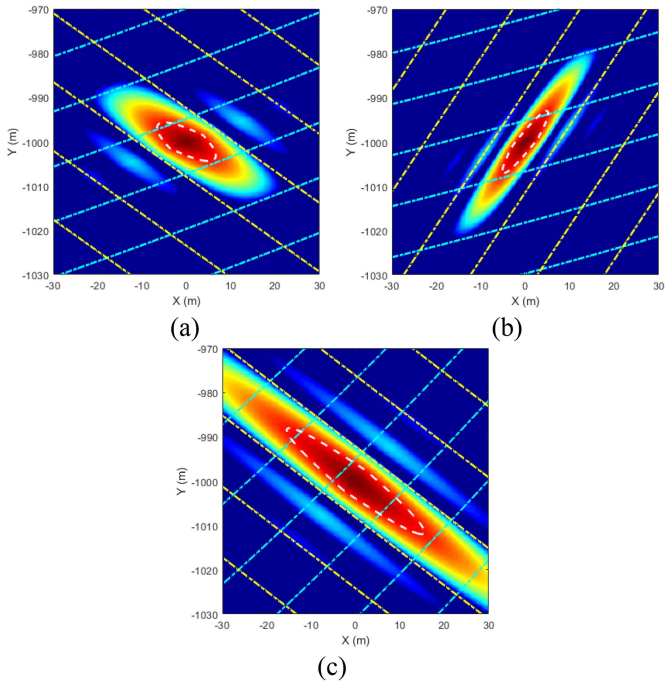

Fig. 2. Bistatic GAFs concerning. (a) First satellite. (b) Second satellite. (c) Third satellite.

Fig. 2 shows a set of bistatic GAFs concerning the three considered satellite transmitters. The iso-range and iso-Doppler lines are simultaneously given in the figures by the cyan and yellow dashdot lines. It is seen that the spatial resolution of the same scatterer varies with its transmitter due to different bistatic geometries. -3 dB cuts of the GAFs (refer to as resolution cell) are simultaneously presented in the figures, as indicated by the white dash lines. A sufficiently long synthetic aperture time ensures a fine azimuth resolution, while only moderate range resolution is achieved due to the insufficient signal bandwidth. The area of resolution cell can be used to quantitatively compare the quality of different radar images. Here, the areas are calculated as 68.4, 45.6, and 182.44 m^2, respectively.

Then, a subset of the bistatic GAFs can be noncoherently combined to form the multistatic GAF. Taking the first satellite

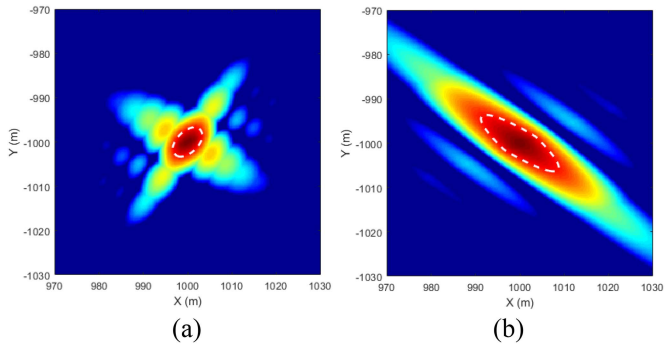

Fig. 3. Multistatic GAFs obtained by combining. (a) First and second satellites. (b) First and third satellites.

as a benchmark, the multistatic GAFs acquired by adding this benchmark with the other two satellites are presented in Fig. 3. The resolution cells are also given by the white dash lines in both figures, where the areas equal to 30.2 and 98.1 m^2, respectively. Compared with the benchmark in Fig. 2(a), it is found that the spatial resolution of a multistatic radar image can be potentially improved by fusing bistatic images concerning different transmitters [see Fig. 3(a)]. But, the improvement does not always work [see Fig. 3(b)]. Although here the multistatic GAF is obtained by combining two bistatic GAFs, the same results can be observed in the case of using bistatic GAFs involving more than two transmitters. Therefore, it can be concluded that the spatial resolution of the multistatic image is strictly dependent on the transmitters used for imaging purpose.

III. Optimal Imaging Method

In this section, the natural multistatic configuration of GNSS-based passive SAR is utilized to obtain an optimal radar image of a large field-of-view. The main processing chain contains the transmitters selection and optimal radar image formation, as described in detail below.

Although the received signals are continuous in time, they are preliminarily reformatted into fast-time and slow-time domain according to an equivalent pulse repetition interval (PRI) [15]. At first, signal synchronization method as described in [25] is performed. The delay, Doppler, and navigation message are extracted from the direct signal, and a noise-free replica (refer to as a reference signal) is generated [25]. By cross-correlation the echo with the reference signal, signal synchronization, as well as range compression, can be achieved. Without loss of generality, we assume a point scatterer located at $\mathbf{A} = (x, y)$ in the same horizontal plane as the fixed receiver. After signal synchronization, the echo from the scatterer can be modeled as

$$s_k(\tau, \eta; x, y) = \sigma_k(x, y)\,\mathrm{rect}\left(\frac{\eta}{T_a}\right)\rho\left[\tau - \frac{R_k(\eta; x, y)}{c}\right] \times \exp\left\{-j\frac{2\pi}{\lambda}R_k(\eta; x, y)\right\} \tag{3}$$

where τ and η denote the fast-time and slow-time. σ_k is the scatterer reflectivity. T_a is the synthetic aperture time. R_k is the difference in propagation path between the reflected signal and the direct signal (refer to as differential bistatic range). That is $R_k = R_{T,k} + R_R - R_{b,k}$, where $R_{b,k}$ is the baseline between satellite and receiver, and $R_{T,k}$ and R_R are the distances from the scatterer respectively to the satellite and the receiver.

Thus, the reflected echo from the surveyed area after signal synchronization is given as

$$S_k(\tau, \eta) = \iint_{\Omega} s_k(\tau, \eta; x, y)\,dxdy \tag{4}$$

where Ω is the observed area.

Then, with respect to each scatterer, a set of satellites used for the imaging process are selected from all the alternatives. In this article, the utilization of the multistatic configuration aims to minimize the spatial resolution of the final radar image. Here, the spatial resolution of a multistatic image is theoretically evaluated by the multistatic GAF, which is obtained by adding the amplitudes of bistatic GAFs concerning the used satellites. That is, the multistatic GAF is given by

$$\chi(\mathbf{A}, \mathbf{B}) = \sum_{k=Ks}\left|\rho\left(\frac{(\mathbf{\Phi_{TA},}_k + \mathbf{\Phi_{RA}})(\mathbf{B}-\mathbf{A})^{\mathbf{T}}}{c}\right)m \times \left(\frac{\boldsymbol{\omega}_{\mathbf{TA},k}(\mathbf{B}-\mathbf{A})^{\mathbf{T}}}{\lambda}\right)\right| \tag{5}$$

where Ks is the index set of the used satellites, and it can be of any size and in any combination. We turn to numerical method to obtain the value of the resolution cell area concerning this scatterer, which is denoted by $S_a(x, y; Ks)$.

As can be seen in Section II, the spatial resolution cell of a multistatic GAF is possibly reduced compared to a bistatic GAF. But not every combination of bistatic GAFs provides a smaller resolution cell. Thus, not all the available satellites in view are used as opportunistic transmitters for the GNSS-based passive SAR to improve the image quality. Furthermore, since the GAF is space-variant, it can be inferred that different sets of the used transmitters need to be determined for different scatterers in a large field-of-view. In addition, it is also deduced from the analyses in Section II that the selection of transmitter set is only determined by the view angle ϕ_A. Using the minimal spatial resolution cell as the optimal criterion, the satellites used for the imaging purpose are selected as

$$\hat{Ks}(\phi_A) = \arg\min_{Ks} S_a(\cos(\phi_A), \sin(\phi_A); Ks). \tag{6}$$

To solve this optimization problem, *K* decision variables are defined as $\mathbf{I}(\phi_A) = [i_{\phi_A,1}, i_{\phi_A,2}, \ldots, i_{\phi_A,k}, \ldots i_{\phi_A,K}]$, where $i_{\phi_A,k} \in \{0, 1\}$ is the selection identifier. If $i_{\phi_A,k} = 1$, the *k*th satellite is selected as an element of the transmitter set, while if $i_{\phi_A,k} = 0$, this satellite is rejected. The optimal $\mathbf{I}(\phi_A)$ can be obtained via some genetic or evolutionary algorithms. In this article, a population-based stochastic optimization algorithm named particle swarm optimization (PSO) is employed [26]. The PSO population with particles is randomly generated, after which the particles fly toward the direction guided by their personal best and the global best. After iteration, the position where the particles converged represents the optimized solution

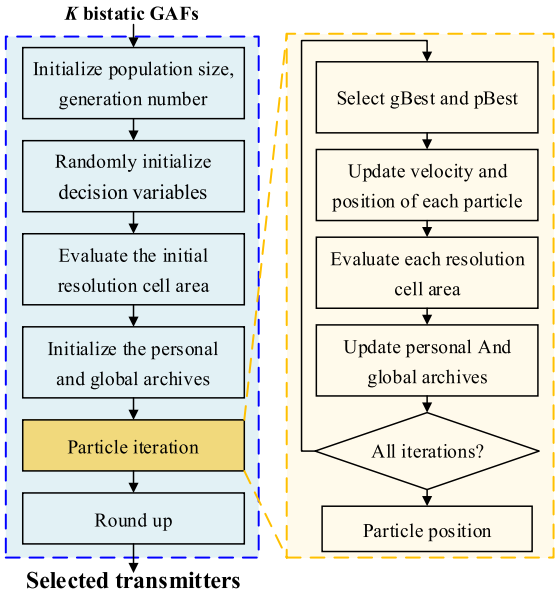

Fig. 4. Procedure of transmitter set determination.

$\hat{\mathbf{I}}(\phi_A)$. The procedure of the transmitter set decision based on PSO is given in Fig. 4.

Finally, the SAR image is formed using the selected satellite transmitters. During the imaging processing, the long-time echo concerning the same transmitter is coherently combined, while the echoes pertaining to the multiple satellites are noncoherently combined. Based on the processing chain of the back-projection algorithm (BPA) [27], each pixel in the imaging plane is calculated according to the equation as

$$f(x,y) = \frac{1}{N} \sum_{k=\hat{K}s(\tan^{-1}(y/x))} \left| \int_{\eta} S_k(\tau,\eta) \times \exp\left\{ j\frac{2\pi}{\lambda} R_k(\eta;x,y) \right\} d\eta \right| = \frac{\sum_k \hat{i}_{\tan^{-1}(y/x),k} \cdot \left| \int_{\eta} S_k(\tau,\eta) \times \exp\left\{ j\frac{2\pi}{\lambda} R_k(\eta;x,y) \right\} d\eta \right|}{\left\| \hat{\mathbf{I}}(\tan^{-1}(y/x)) \right\|_0} \tag{7}$$

where $R_k(\eta;x,y)$ is the differential bistatic range history of the pixel concerning the kth satellite transmitter and the fixed receive, and N is the size of the selected transmitter set. $\|\cdot\|_0$ is the $L0$ norm. Here, $\tan^{-1}(y/x)$ is used to calculated the corresponding view angle. It is noted that generally the grids of the BPA should be smaller than the spatial resolution [28]. In the passive SAR system based on GNSS transmitters, the bistatic azimuth resolution is usually smaller than the range resolution. Therefore, the spatial resolution cell of the GNSS-based multistatic SAR is mainly determined by the azimuth resolution. That is, the grids of BPA are determined by the minimal azimuth resolution.

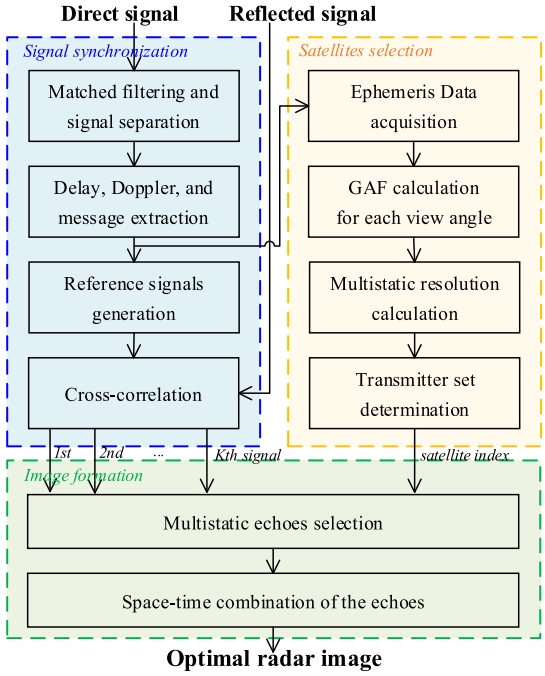

Fig. 5. Scheme of the proposed imaging method.

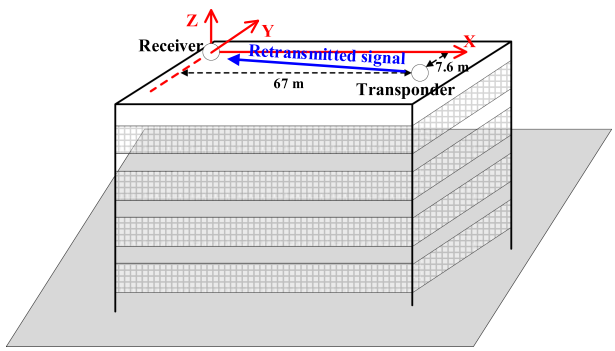

Fig. 6. Experiment scenario using a signal transponder.

To sum up, the scheme of the optimal imaging method for large field-of-view using GNSS-based SAR is shown in Fig. 5.

IV. Experimental Results

In this section, the proposed imaging method is applied to the experimental data collected from different scenarios to verify its effectiveness. The first experiment was carried out using a GNSS signal transponder as a strong point target, and in the other experiment, the scene with a large field-of-view was covered by the receiver.

A. Point Target

In this experiment, the data was collected using BeiDou satellites as transmitters of opportunity. As shown in Fig. 6, the transponder with an amplifier and the passive receiver was fixed on the roof of a building. Constituting a local reference system using the receiver as origin, the position of the transponder can be expressed as (67, −7.6) m. During the data acquisition, the

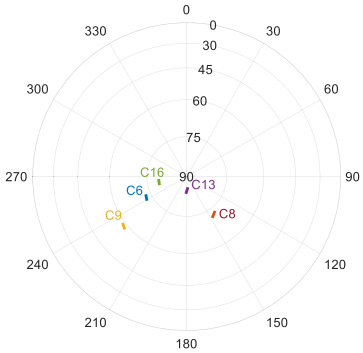

Fig. 7. Skymap of the considered satellites in the first experiment.

TABLE II
PARAMETERS OF THE FIRST EXPERIMENT

Parameters		Value
BeiDou C06	Azimuth angle	238.72–246.59°
	Elevation angle	72.73–73.40°
BeiDou C08	Azimuth angle	140.48–148.32°
	Elevation angle	73.46–71.93°
BeiDou C09	Azimuth angle	229.51–234.16°
	Elevation angle	59.72–60.57°
BeiDou C13	Azimuth angle	173.53–182.90°
	Elevation angle	86.00–83.59°
BeiDou C16	Azimuth angle	252.53–265.14°
	Elevation angle	79.38–79.50°
Carrier frequency		1268.520 MHz
Signal chip rate		10.23 MHz
Sampling rate		50 MHz
Dwell time		600 s
Equivalent PRI		1 ms

BeiDou B3I signals were recorded by the transponder [29]. After demodulation and remodulation, the power-amplified signals of opportunity were retransmitted from the transponder and were immediately received by the receiver through the surveillance antenna pointing to the transponder. At the same time, the direct signals from the BeiDou satellites were received by the receiver through the reference antenna pointing to the sky. In this way, a strong point target can be simulated, so that the imaging performance of the proposed method can be quantitatively evaluated.

In this experiment, the signals from five BeiDou satellites were retransmitted by the transponder. The retransmitted signals and the corresponding direct signals concerning the five satellites were simultaneously collected by the receiver. All the considered satellites were in IGSO with an altitude of 35786 km. During the data acquisition, the skymap of these satellites is shown in Fig. 7, and the parameters are given in Table II.

Since the BeiDou system utilizes the code division multiple access technique, signals from different satellites can be distinguished and extracted via match filter banks with pseudorandom codes. After matched filtering, the first 5 s signals recorded by the reference and surveillance antennas concerning BeiDou C06 are presented in Fig. 8. The color scale is in dB, where 0 dB represents the mean noise power. In Fig. 8(a), the direct signal is isolated from the noise background owing to its sufficient SNR, which is the premise of signal synchronization. For comparison, the direct signal also exhibits in Fig. 8(b), as it is concurrently recorded in the surveillance antenna. In addition, the retransmitted BeiDou signal is clearly visible in Fig. 8(b), so it is reasonable to treat it as an echo from a strong point target. The shift between the direct signal and the retransmitted signal is caused by the different propagation paths and the processing delay of the transponder.

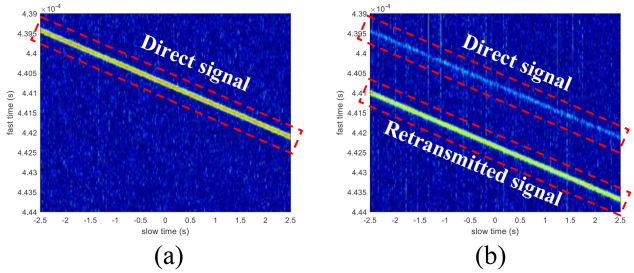

Fig. 8. Signals after matched filtering pertaining to (a) reference antenna and (b) surveillance antenna.

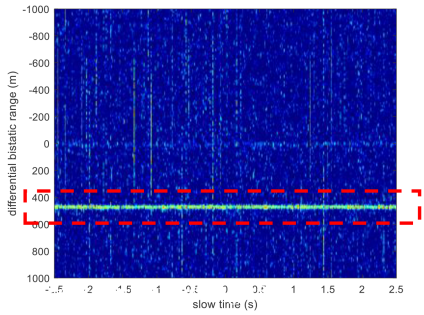

Fig. 9. Result after signal synchronization.

Then, for signal synchronization purpose, a reference signal is generated from Fig. 8(a). After cross-correlation of the reference signal and the received echo, the corresponding result is shown in Fig. 9. The Y-axis represents the differential bistatic range, where the direct signal always presents at zero lines. It is seen that the amplitude of the retransmitted signal is much larger than that of the direct signal. Thus, the direct signal has no effect on the subsequent imaging processing.

The entire dwell time on the transponder is 10 min in this experiment. Using the satellites' trajectories accurately obtained from the ephemeris data, the bistatic GAFs concerning the point where the transponder is located are shown in Fig. 10. The figures are presented in dB, where 0 dB represents the maximum intensity and the dynamic range is clipped to 20 dB. The resolution cell (i.e., −3 dB cut) is also given in each GAF, marked by the white dash line. The theoretical imaging performances quantitatively evaluated by spatial resolutions with

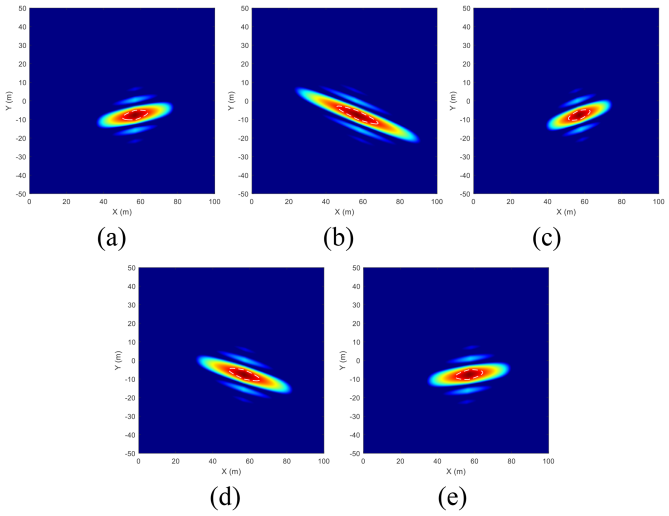

Fig. 10. Bistatic GAFs concerning. (a) C06. (b) C08. (c) C09. (d) C13. (e) C16.

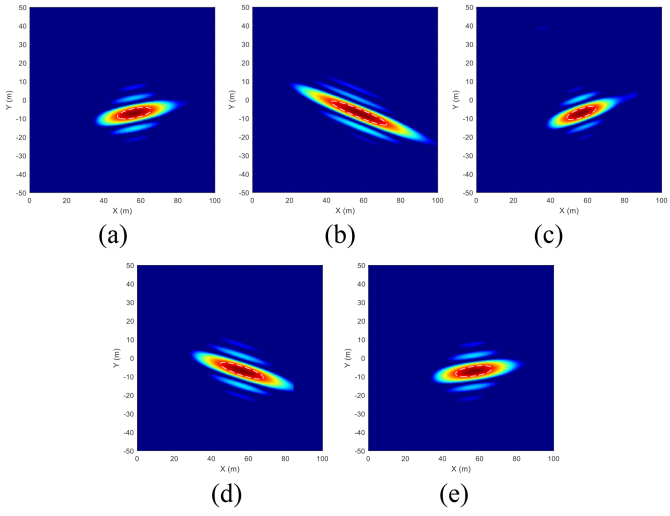

Fig. 11. Bistatic images concerning. (a) C06. (b) C08. (c) C09. (d) C13. (e) C16.

TABLE III
IMAGING PERFORMANCE IN THEORY

Satellite index	Spatial resolution		
	Range resolution	Azimuth resolution	Resolution cell area
C06	13.71 m	4.96 m	48.27 m^2
C08	20.85 m	4.26 m	71.39 m^2
C09	12.16 m	4.67 m	40.53 m^2
C13	17.34 m	4.69 m	58.91 m^2
C16	14.62 m	5.17 m	54.23 m^2

TABLE IV
IMAGING PERFORMANCE OF A POINT TARGET

Satellite index	Spatial resolution		
	Range resolution	Azimuth resolution	Resolution cell area
C06	18.14 m	5.22 m	71.73 m^2
C08	28.00 m	4.41 m	99.58 m^2
C09	16.33 m	4.84 m	61.48 m^2
C13	23.82 m	4.89 m	90.50 m^2
C16	19.48 m	5.36 m	68.23 m^2

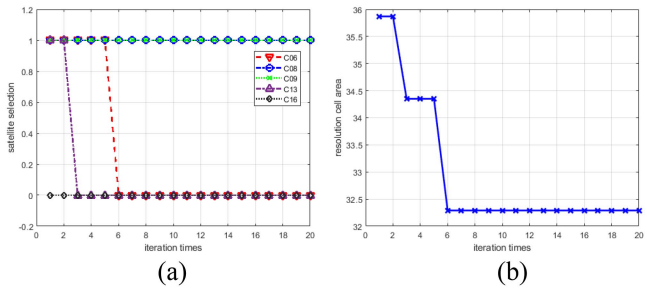

Fig. 12. Solving process during the iterations. (a) Satellite selection. (b) Theoretical resolution cell area.

respect to each bistatic geometry are given in Table III. The spatial resolution changes with the transmitter. In addition, a moderate range resolution with a value of more than 10 m can be observed in each bistatic case owing to the limited BeiDou signal bandwidth.

In theory, the imaging result of an independent point target should be consistent with its GAF. For comparison, bistatic images are formed using the experimental data. It is noted that, there is inevitably a processing delay caused by the transponder in the received data. Thus, the imaging processing is performed after delay compensation. By performing the BPA on the range-compressed data, the obtained bistatic images are presented in Fig. 11, which are in line with the theoretical expectations in Fig. 10. The spatial resolutions evaluated from these radar images are given in Table IV. It is pointed out that, the cross-correlation between the generated ranging code and recorded signals from the other satellites can be an interference to range-compressed result, which causes the differences in range resolution values between theoretical and experimental results.

Then, the PSO algorithm is performed to determine the optimal transmitter set based on the theoretical GAFs. The population size of the PSO is set as 10 to show the evolution during the iterations, and the generation number is set as 20. The valid search space is set as [01]. The PSO-based solving process is shown in Fig. 12. It is found that with the updating of the particles, the population evolves to find a better solution with a smaller resolution cell area. After the iteration, the selection identifiers of C08 and C09 are set to be 1 (i.e., the final optimal solution is obtained as [01,10,0]). Therefore, the C08 and C09 satellites are selected as the transmitters of opportunity for the optimal imaging purpose, which expects to obtain the image with minimal resolution cell. The corresponding imaging result is shown in Fig. 13. The resolution cell area is 44.82 m^2, which

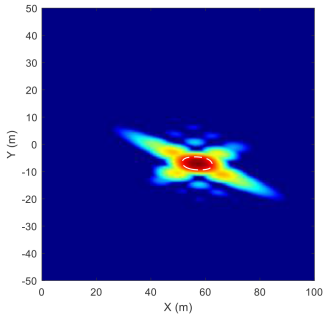

Fig. 13. Final image with a minimal resolution cell.

(a)

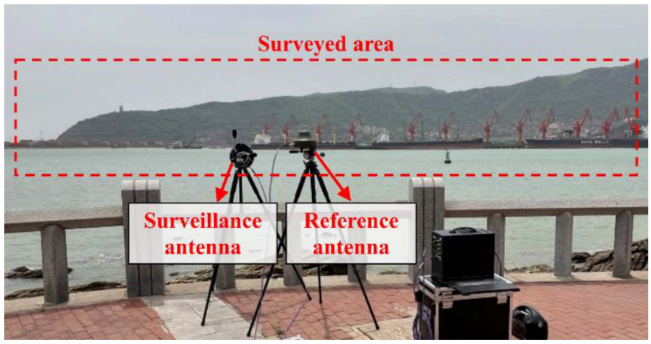

(b)

Fig. 14. GNSS-based SAR experiment. (a) Imaging scenario. (b) Receiving system.

is apparently lower than that in each of the bistatic geometries. Thus, it can be concluded that the final image provides a better imaging performance.

B. Large Field-of-View

In this section, the effectiveness of the proposed imaging method is further verified by performing it on the experimental data received from a large field-of-view. The experiment was carried out at Lianyungang port in China. Fig. 14(a) shows the optical photograph of the experimental scenario cropped from Google Earth, and the dimensions of the scenario are 2.5 km $\times$ 5 km. Four main target areas in this scenario are highlighted with the white rectangles. The areas 1, 2, and 3 are the wharves, and the area 4 is the mountainous area surrounded by roads. The passive receiver equipped with two antennas was fixed at the coast [see Fig. 14(b)]. One of the antennas stared south, while the other pointed to the sky, serving as surveillance and reference antennas, respectively. Both antennas are identical with a low gain of 5 dB. And the large beamwidth ensures that all the four target areas can be simultaneously covered by the receiver. In Fig. 14(b), the cranes in the wharves and the mountainous area have also been photographed.

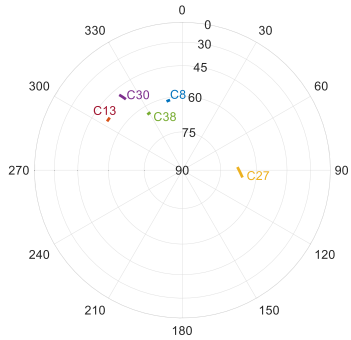

Fig. 15. Skymap of the considered satellites in the second experiment.

TABLE V
PARAMETERS OF THE SECOND EXPERIMENT

Parameters		Value
BeiDou C08	Azimuth angle	347.04–350.04 °
	Elevation angle	62.66–62.38 °
BeiDou C13	Azimuth angle	302.97–305.91 °
	Elevation angle	55.24–55.27 °
BeiDou C27	Azimuth angle	86.75–96.90 °
	Elevation angle	68.65–66.55 °
BeiDou C30	Azimuth angle	320.03–321.46 °
	Elevation angle	51.91–54.85 °
BeiDou C38	Azimuth angle	327.83–331.03 °
	Elevation angle	64.52–64.41 °
Sampling rate		50 MHz
Dwell time		600 s
Equivalent PRI		1 ms

In this experiment, the dataset was also collected using BeiDou satellites as illuminators of opportunity, and the BeiDou B3I signal with a chip rate of 10.23 MHz was recorded by the receiver. The skymap of the utilized satellites during data acquisition is shown in Fig. 15, and the corresponding parameters are given in Table V. The BeiDou C27 and C30 are in MEO with a satellite altitude of 21528 km, while C08, C13, and C38 are in IGSO with a satellite altitude of 35786 km.

After signal synchronization and range compression, the first 5 s data recorded in the surveillance antenna pertaining to BeiDou C27 is presented in Fig. 16(a). Only the direct signal along the zero bistatic line can be observed in this figure, while the reflected signal is invisible owing to its poor power. The direct signal concurrently recorded in the surveillance antenna

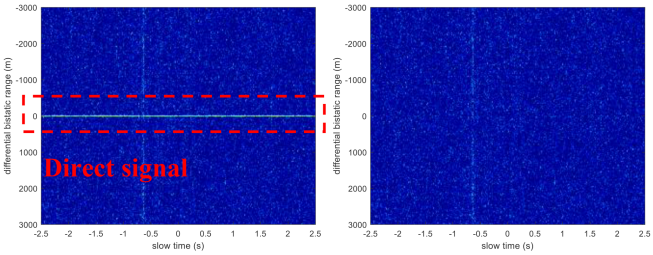

Fig. 16. Range-compressed data. (a) Before direct signal cancellation. (b) After direct signal cancellation.

will severely interfere with the subsequent imaging processing. To excise this interference, here the extensive cancellation algorithm (ECA) is proactively applied to the received data, which intends to remove the disturbance by resorting to the reference signal generated from the reference antenna [30]. After the ECA, the corresponding result is shown in Fig. 16(b), from which the direct signal suppression can be observed.

In order to guarantee a sufficient SNR for the radar image, a data stream of 10 min is used for the imaging processing. By means of the BPA, the formed bistatic images concerning the five BeiDou transmitters are presented in Fig. 17. The grids of the BPA are set to be 2 m, which is slightly smaller than the theoretical azimuth resolution of the bistatic configuration with a MEO transmitter. It is pointed out that, hereinafter the color scale of radar image is in dB. All the images are normalized to the mean noise power, and the value can be calculated from the noise area in bistatic image where target areas are not contained. Typically, the noise amplitude complies with Rayleigh distribution. To make 99.5% noise invisible in bistatic images, the display threshold of each image is set to be 7.2 dB. To clearly present the target outline, each image is displayed with a color scale with 3 dB of dynamic. That is, hereinafter the dynamic range of radar image is set as [7.2, 10.2] dB. For better presentation, the radar images are superimposed on the photograph of the surveyed area in Fig. 14(a). Fig. 17 shows a good coincidence between the bistatic images and the optical scenario, where the four main target areas are visible in the radar images (see white rectangles). However, due to the large field-of-view, the space-variant resolution is apparent in the bistatic images. Not every target area in the scene can acquire a fine spatial resolution with the bistatic geometries. In specific, there is a sufficient difference in view angle between the area 1 and area 3. In Fig. 17(a), (b), and (e), the outline information of the wharf in area 3 can be clearly observed which indicates its fine spatial resolution, while in area 1 a poor resolution can be observed. Similar results can also be observed in Fig. 17(c) and (d), where the wharves in area 1 are outlined in radar images and the area 3 is blurry. Therefore, it is found that a radar image with fine spatial resolution can hardly be achieved for a scene with a large field-of-view using the bistatic GNSS-based SAR.

For comparison with the proposed method, the multistatic image is first achieved by fully combining all the five bistatic images, and the corresponding result is given in Fig. 18. The

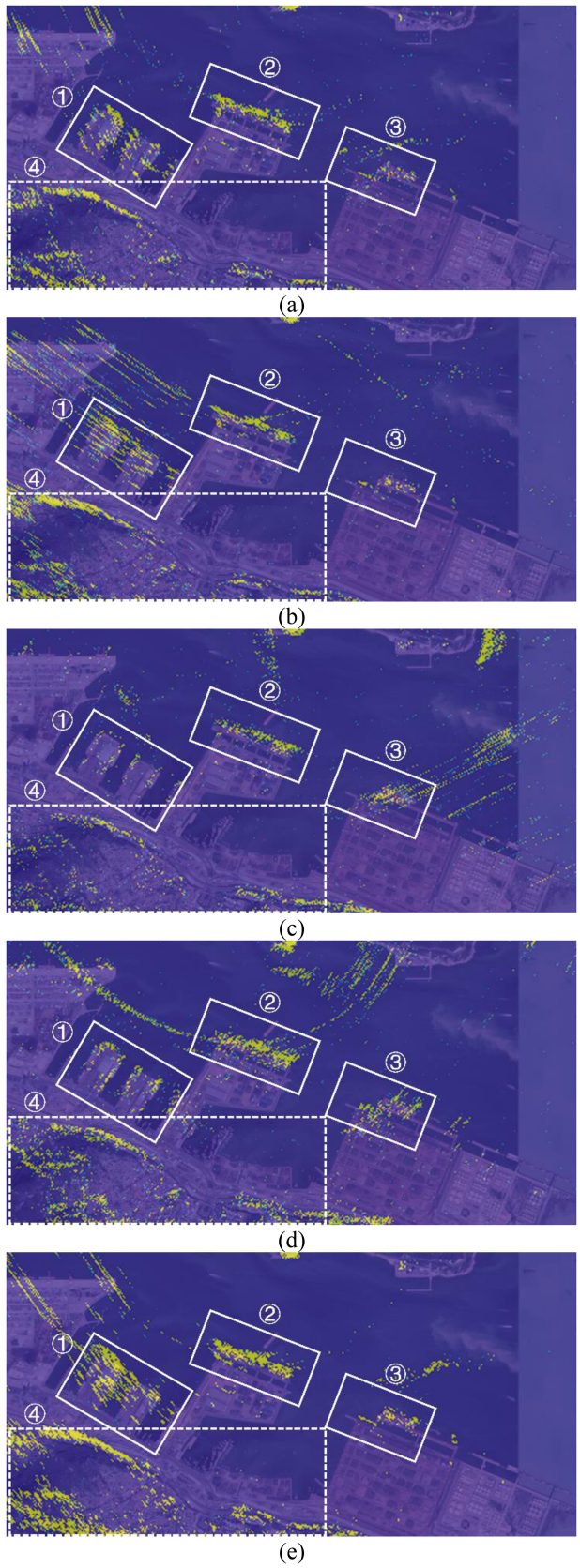

Fig. 17. Bistatic images of the large field-of-view concerning. (a) C08. (b) C13. (c) C27. (d) C30. (e) C38.

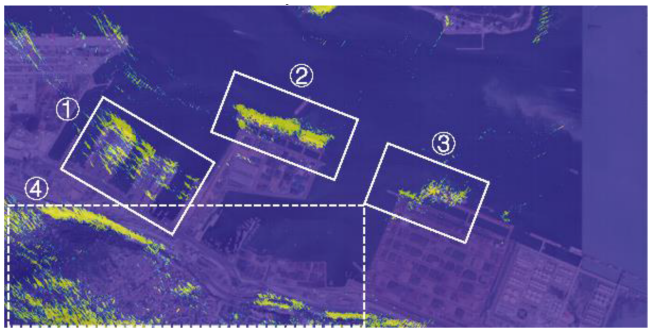

Fig. 18. Multistatic image obtained by full combination of the bistatic images.

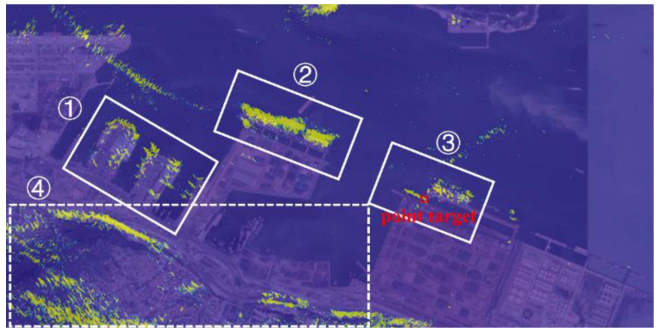

Fig. 20. Final radar image of the large field-of-view.

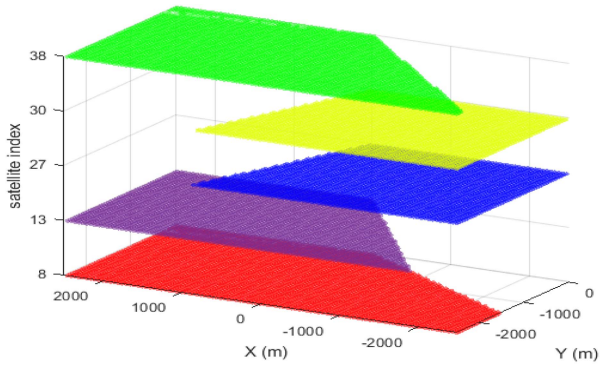

Fig. 19. Selection of the satellite transmitters.

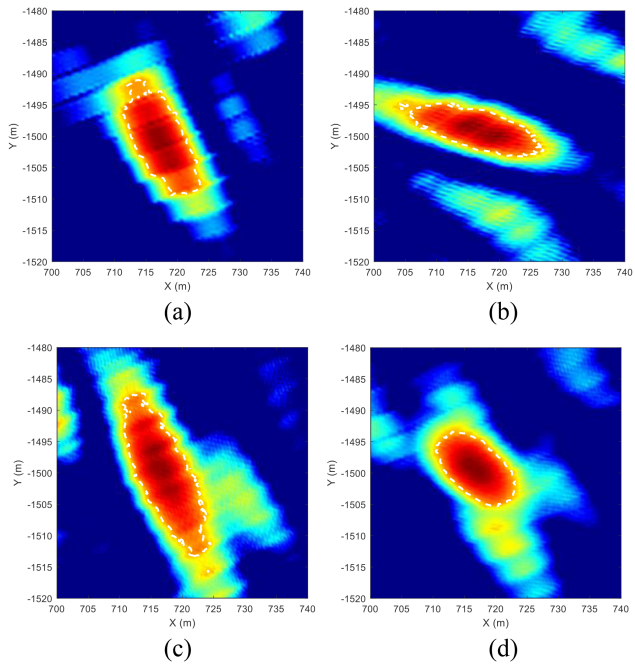

Fig. 21. Images of the point scatterer concerning. (a) C08. (b) C13. (c) C38. (d) Fusion result.

inferior imaging results in bistatic cases are still maintained in this multistatic image, causing a degeneration of the imaging performance. This is evident in area 1 in Fig. 18, where the outline of the wharf is blurry.

Then, the optimal imaging processing is applied to the same data. The multistatic configuration of the GNSS-based passive SAR is utilized to provide a minimal spatial resolution for every scatterer in the large field-of-view. After PSO, the selection of the used satellite transmitters for each pixel in the imaging plane is shown in Fig. 19. The Z-axis represents the satellite index, and thus it is observed that there are five slices along the Z-axis. For the sake of better presentation, different colors are utilized to represent the different satellites. At each slice, the colored area denotes that this satellite is used as the transmitter for the imaging purpose concerning this pixel, while the blank area denotes that this satellite is unemployed. Subsequently, the radar image simultaneously using the multiple satellites are formed, and the final imaging result is shown in Fig. 20. It is found that the outlines of the wharves in the area 1, 2, and 3 can be clearly observed at the same time. In the area 4, the edges of the mountain match the optical map. All target areas over the large field-of-view are well imaged, which is difficult to realize in the case of each bistatic image and the case of full bistatic images combination. Thus, it is concluded that an improved radar image can be achieved via the proposed method.

Finally, a point target located at (717, −1500) m (see the red rectangle in Fig. 20) is extracted from the imaging results for the resolution evaluation. According to Fig. 19, the echoes from BeiDou C08, C13, and C38 are utilized for the imaging of this point scatterer. After extraction and interpolation, the bistatic images of this point scatterer concerning the three selected transmitters are presented in Fig. 21(a)–(c). The −3 dB cut of each image is simultaneously given and marked by the white dash line. The resolution cell areas of these bistatic images are quantitatively evaluated as 121.01, 100.15, and 164.78 m^2, respectively. By comparison, the point scatterer imaging result via the proposed method is shown in Fig. 21(d). The resolution cell area of this imagery is obtained as 93.11 m^2, which is lower than that of each bistatic image. Thus, the resolution improvement of the proposed method can also be quantitatively proved by the experimental results.

V. Conclusion

This article proposes an optimal GNSS-based passive SAR imaging method for a large field-of-view. Only a moderate

range resolution is provided by GNSS signals. And the notable space-variant resolution in the large field-of-view deteriorates the passive SAR imaging performance. To address these problems, the inherent multistatic nature of GNSS is utilized. On the one hand, with respect to the large field-of-view, the multiple available satellites ensure an acceptable spatial resolution for every scatter in the scene since the different GNSS transmitters can be used. On the other hand, with respect to a scatterer, the orientations and values of bistatic resolution cells pertaining to multiple GNSS transmitters are different. The combination of different transmitters has the opportunity to reduce the resolution cell. In this article, the transmitter set for each scatterer in the large field-of-view is seriatim determined according to the criterion of a minimal resolution cell. The final radar image is formed by combining the echoes from the corresponding transmitters. The effectiveness of the proposed method is demonstrated using two experimental datasets. In the first experiment, a transponder was placed in the surveyed area, which can be treated as a strong point target. The processing results quantitatively show the resolution improvement. And in the other experiment, the large field-of-view imaging capability of the proposed method is illustrated, since the surveyed area with a large field-of-view has been well imaged using the BeiDou-based passive SAR system.

REFERENCES

[1] A. Reigber et al., "Very-High-Resolution airborne synthetic aperture radar imaging: Signal processing and applications," *Proc. IEEE*, vol. 101, no. 3, pp. 759–783, Mar. 2013.

[2] H. D. Griffiths, "From a different perspective: Principles, practice and potential of bistatic radar," in *Proc. Int. Conf. Radar*, 2003, pp. 1–7.

[3] Z. Li et al., "Bistatic SAR clutter-ridge matched STAP method for Non-stationary clutter suppression," *IEEE Trans. Geosci. Remote Sens.*, vol. 60, 2022, Art. no. 5216914, doi: 10.1109/TGRS.2021.3125043.

[4] H. Kuschel, M. Ummenhofer, P. Lombardo, F. Colone, and C. Bongioanni, "Passive radar components of ARGUS 3D," *IEEE Aerosp. Electron. Syst. Mag.*, vol. 29, no. 3, pp. 15–25, Mar. 2014.

[5] Z. Li et al., "Hybrid SAR-ISAR image formation via joint FrFT-WVD processing for BFSAR ship target high-resolution imaging," *IEEE Trans. Geosci. Remote Sens.*, vol. 60, 2022, Art. no. 5215713, doi: 10.1109/TGRS.2021.3117280.

[6] Z. Li, S. Li, Z. Liu, H. Yang, J. Wu, and J. Yang, "Bistatic forward looking SAR MP-DPCA method for spacetime extension clutter suppression," *IEEE Trans. Geosci. Remote Sens.*, vol. 58, no. 9, pp. 6565–6579, Sep. 2020.

[7] L. M. H. Ulander, P.-O. Frölind, A. Gustavsson, R. Ragnarsson, and G. Stenström, "Airborne passive SAR imaging based on DVB-T signals," in *Proc. IEEE Int. Geosci. Remote Sens. Symp.*, 2017, pp. 2408–2411.

[8] D. Gromek, K. Kulpa, and P. Samczyński, "Experimental results of passive SAR imaging using DVB-T illuminators of opportunity," *IEEE Geosci. Remote Sens. Lett.*, vol. 13, no. 8, pp. 1124–1128, Aug. 2016.

[9] P.-O. Frölind, "Results of airborne passive SAR ground and sea target imaging using DVB-T signals," in *Proc. IEEE Radar Conf.*, 2016, pp. 1–4.

[10] K. Radecki, P. Samczyński, D. Gromek, and K. Kulpa, "The use of barycentric BPA for passive SAR imaging," in *Proc. 21st Int. Radar Symp.*, 2020, pp. 236–239.

[11] Z. Li, F. Santi, D. Pastina, and P. Lombardo, "Passive radar array with low-power satellite illuminators based on fractional Fourier transform," *IEEE Sensors J.*, vol. 17, no. 24, pp. 8378–8394, Dec. 2017.

[12] M. Antoniou and M. Cherniakov, "GNSS-based bistatic SAR: A signal processing view," in *Proc. EURASIP J. Adv. Signal Process.*, 2013, pp. 1–16.

[13] Z. Li, F. Santi, D. Pastina, and P. Lombardo, "Multi-frame fractional fourier transform technique for moving target detection with space-based passive radar," *IET Radar, Sonar Navigation*, vol. 11, no. 5, pp. 822–828, 2017.

[14] C. Huang, Z. Li, H. An, Z. Sun, J. Wu, and J. Yang, "Passive multistatic radar imaging of vessel target using GNSS satellites of opportunity," *IEEE Trans. Geosci. Remote Sens.*, vol. 60, 2022, Art. no. 5116416, doi: 10.1109/TGRS.2022.3195993.

[15] Z. Li, C. Huang, Z. Sun, H. An, J. Wu, and J. Yang, "BeiDou-Based passive multistatic radar maritime moving target detection technique via space–time hybrid integration processing," *IEEE Trans. Geosci. Remote Sens.*, vol. 60, 2022, Art. no. 5802313, doi: 10.1109/TGRS.2021.3128650.

[16] C. Huang et al., "BeiDou-Based passive radar vessel target detection: Method and experiment via long-time optimized integration," *Remote Sens.*, vol. 13, no. 19, pp. 3933, Sep. 2021.

[17] Z. Liu et al., "Optimally matched space-time filtering technique for BFSAR nonstationary clutter suppression," *IEEE Trans. Geosci. Remote Sens.*, vol. 60, 2022, Art. no. 5210617, doi: 10.1109/TGRS.2021.3090462.

[18] Y. Wang, Z. Ding, P. Xu, K. Chen, T. Zeng, and T. Long, "Strip layering diagram-based optimum continuously varying pulse interval sequence design for extremely high-resolution spaceborne sliding spotlight SAR," *IEEE Trans. Geosci. Remote Sens.*, vol. 59, no. 8, pp. 6751–6770, Aug. 2021.

[19] Y. Hai et al., "Microwave photonic SAR High-precision imaging based on optimal subaperture division," *IEEE Trans. Geosci. Remote Sens.*, vol. 60, 2022, Art. no. 5232317, doi: 10.1109/TGRS.2022.3192583.

[20] T. Zeng, T. Zhang, W. Tian, C. Hu, and X. Yang, "Bistatic SAR imaging processing and experiment results using beidou-2/Compass-2 as illuminator of opportunity and a fixed receiver," in *Proc. IEEE 5th Asia-Pac. Conf. Synthetic Aperture Radar*, 2015, pp. 302–3053.

[21] U. Nithirochananont, M. Antoniou, and M. Cherniakov, "Passive Multistatic SAR – experimental results," *IET Radar, Sonar Navig.*, vol. 13, no. 2, pp. 222–228, 2019.

[22] F. Santi, M. Antoniou, and D. Pastina, "Point spread function analysis for GNSS-Based multistatic SAR," *IEEE Geosci. Remote Sens. Lett.*, vol. 12, no. 2, pp. 304–308, Feb. 2015.

[23] T. Zeng et al., "Multiangle BSAR imaging based on beidou-2 navigation satellite system: Experiments and preliminary results," *IEEE Trans. Geosci. Remote Sens.*, vol. 53, no. 10, pp. 5760–5773, Oct. 2015.

[24] T. Zeng, M. Cherniakov, and T. Long, "Generalized approach to resolution analysis in BSAR," *IEEE Trans. Aerosp. Electron. Syst.*, vol. 41, no. 2, pp. 461–474, Apr. 2005.

[25] H. Ma et al., "Maritime moving target indication using passive GNSS-Based bistatic radar," *IEEE Trans. Aerosp. Electron. Syst.*, vol. 54, no. 1, pp. 115–130, Feb. 2018.

[26] Z. Li, J. Wu, J. Yang, and Z. Liu, *Bistatic SAR Clutter Suppression: Theory Method and Experiment*. Berlin, Germany: Springer, 2022.

[27] D. L. N. Hettiarachchi and E. J. Balster, "Fixed-Point processing of the SAR back-projection algorithm on FPGA," *IEEE J. Sel. Topics Appl. Earth Observ. Remote Sens.*, vol. 14, pp. 10889–10902, 2021.

[28] O. Tulgar and A. Arif Ergin, "Improved pencil back-projection method with image segmentation for far-field/near-field SAR imaging and RCS extraction," *IEEE Trans. Antennas Propag.*, vol. 63, no. 6, pp. 2572–2584, Jun. 2015.

[29] China Satellite Navigation Office, "BeiDou navigation satellite system signal in space interface control document," in *Open Service Signal B3I (Version 1.0)*, Sacramento, CA, USA: CSNO, 2018.

[30] F. Colone, D. W. O'Hagan, P. Lombardo, and C. J. Baker, "A multistage processing algorithm for disturbance removal and target detection in passive bistatic radar," *IEEE Trans. Aerosp. Electron. Syst.*, vol. 45, no. 2, pp. 698–722, Apr. 2009.

Chuan Huang (Student Member, IEEE) received the B.S. degree in electronic engineering in 2017 from the University of Electronic Science and Technology of China, Chengdu, China, where he is currently working toward the Ph.D. degree with the School of Information and Communication Engineering.

His research interests include passive radar moving target detection and imaging.

Zhongyu Li (Member, IEEE) received the B.S. and Ph.D. degrees in electronic engineering from the University of Electronic Science and Technology of China (UESTC), Chengdu, China, in 2011 and 2017, respectively.

From 2015 to 2016, he was a Visiting Ph.D. Student with the Department of Information Engineering, Electronics and Telecommunications, Sapienza University of Rome, Rome, Italy. He is currently an Associate Professor with UESTC. His research interests include synthetic aperture radar technology (particular emphasis on synthetic aperture radar ground moving target detection and imaging).

Dr. Li is a Reviewer of the IEEE TRANSACTIONS ON GEOSCIENCE AND REMOTE SENSING, the IEEE GEOSCIENCE AND REMOTE SENSING LETTERS, and the *Journal of Electromagnetic Waves and Applications*.

Hongyang An (Member, IEEE) received the B.S. and Ph.D. degrees in electronic engineering from the University of Electronic Science and Technology of China, Chengdu, China, in 2015 and 2020, respectively.

From 2019 to 2020, he was a Visiting Student with Nanyang Technological University, Singapore. He is with the University of Electronic Science and Technology of China. His research interests include synthetic aperture radar and sparse signal processing.

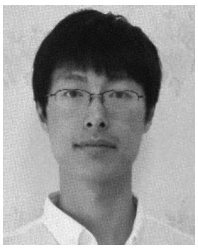

Zhichao Sun (Member, IEEE) received the B.S. and Ph.D. degrees in electronic engineering from the University of Electronic Science and Technology of China (UESTC), Chengdu, China, in 2012 and 2017, respectively.

From September 2016 to September 2017, he was a Visiting Student with the Department of Electrical and Computer Engineering, Oklahoma State University, Stillwater, OK, USA. He was with Huawei Technologies Corporation Ltd., Shenzhen, China, from 2018 to 2019. He is with the UESTC. His research interests include synthetic aperture radar and evolutionary computation applications.

Junjie Wu (Member, IEEE) received the B.S., M.S., and Ph.D. degrees in electronic engineering from the University of Electronic Science and Technology of China (UESTC), in 2004, 2007, and 2013, respectively.

He is currently a Professor with the UESTC, Chengdu, China. From January 2012 to January 2013, he was a Visiting Student with the Department of Electrical and Computer Engineering, Duke University, Durham, NC, USA. His research interests include synthetic aperture radar imaging (particular emphasis on bistatic synthetic aperture radar).

Dr. Wu is the Reviewer for IEEE TRANSACTIONS ON GEOSCIENCE AND REMOTE SENSING, IEEE TRANSACTIONS ON SIGNAL PROCESSING, IEEE JOURNAL OF SELECTED TOPICS IN APPLIED EARTH OBSERVATIONS AND REMOTE SENSING, IEEE JOURNAL OF SELECTED TOPICS IN SIGNAL PROCESSING, IEEE GEOSCIENCE AND REMOTE SENSING LETTERS, *IET Radar, Sonar and Navigation*, and so on.

Jianyu Yang (Member, IEEE) received the B.S. degree in electronic engineering from the National University of Defense Technology, Changsha, China, in 1984 and the M.S. and Ph.D. degrees in electronic engineering from the University of Electronic Science and Technology of China (UESTC), Chengdu, China, in 1987 and 1991, respectively.

He is currently a Professor with the School of Information and Communication Engineering, UESTC. His research interests are mainly in synthetic aperture radar and statistical signal processing.